Journal of Catalysis 286 (2012) 88–94

Contents lists available at SciVerse ScienceDirect

Journal of Catalysis

journal homepage: www.elsevier.com/locate/jcat

Accurate coverage-dependence incorporated into first-principles kinetic models: Catalytic NO oxidation on Pt (1 1 1)

C. Wu [a], D.J. Schmidt [a], C. Wolverton [b], W.F. Schneider [a,c,*]

[a] Department of Chemical and Biomolecular Engineering, University of Notre Dame, Notre Dame, IN 46556, USA
[b] Department of Materials Science and Engineering, Northwestern University, Evanston, IL 60208, USA
[c] Department of Chemistry and Biochemistry, University of Notre Dame, Notre Dame, IN 46556, USA

ARTICLE INFO

Article history:
Received 11 August 2011
Revised 12 October 2011
Accepted 21 October 2011
Available online 26 November 2011

Keywords:
Adsorbate–adsorbate interactions
DFT
Cluster expansion
Rate laws
NO oxidation kinetics
Pt (1 1 1)
O_2 dissociation

ABSTRACT

The coverage of surface adsorbates influences both the number and types of sites available for catalytic reactions at a heterogeneous surface, but accounting for adsorbate–adsorbate interactions and understanding their implications on observed rates remain challenges for simulation. Here, we demonstrate the use of a density functional theory (DFT)-parameterized cluster expansion (CE) to incorporate accurate adsorbate–adsorbate interactions into a surface kinetic model. The distributions of adsorbates and reaction sites at a metal surface as a function of reaction conditions are obtained through Grand Canonical Monte Carlo simulations on the CE Hamiltonian. Reaction rates at those sites are obtained from the CE through a DFT-parameterized Brønsted–Evans–Polyani (BEP) relationship. The approach provides ready access both to steady-state rates and rate derivatives and further provides insight into the microscopic factors that influence observed rate behavior. We demonstrate the approach for steady-state O_2 dissociation at an O-covered Pt (1 1 1) surface—a model for catalytic NO oxidation at this surface—and recover apparent activation energies and rate orders consistent with experiment.

1. Introduction

Density functional theory (DFT) calculations are routinely used today to simulate elementary reactions at a metal surface, and these models have proved highly useful in guiding the design of heterogeneous catalysts [1,2]. Quantitatively relating these results to observed reaction rates, apparent rate orders and activation energies remains more challenging. Even for simple catalytic reactions at an ordered metal surface, lateral interactions between adsorbates can have a strong effect on observed kinetics, both by modifying adsorption and reaction energies and by influencing the distribution of surface adsorbates. Langmuir–Hinshelwood models and mean-field approximations either neglect or average over these interactions [3], but these approximations often break down at real surfaces [4,5]. Lattice-based descriptions combined with kinetic Monte Carlo algorithms provide a more general way of incorporating adsorbate–adsorbate interactions into a kinetic model [6]. For simplicity and generality, however, the interactions are often assumed to be pairwise or are treated semi-empirically [7–14]. Further, the computational expense of kinetic Monte Carlo can make it difficult to extract rate orders and apparent activation energies or to relate them to underlying mechanisms.

Cluster expansions (CEs) offer a more general way of treating the adsorbate interaction problem. CEs applied to adsorption at surfaces expand adsorbate energies in a general basis of pair, triplet, and higher order interactions [15–29]. DFT-parameterized CEs have been successfully used to model the temperature-programmed desorption (TPD) of adsorbates on Ru [15] and Rh [30,31] surfaces, as well as adsorption energies and phase diagrams of oxygen on the Pt (1 1 1) surface [16–19]. To date, however, CEs have not been used to model surface catalytic rates. In this work, we demonstrate the use of the CE for quantitatively describing both the interactions between adsorbates and the rates of surface reactions, an approach that provides easy access to macroscopic kinetic parameters and to the identification of kinetically-relevant sites.

The approach is motivated by the catalytic oxidation of NO to NO_2 over Pt, a reaction of much recent scientific and practical interest [32–36]:

$$2NO + O_2 \overset{Pt}{\rightleftharpoons} 2NO_2 \tag{1}$$

To drive the modestly exothermic reaction toward product, the reaction is carried out under strong oxidizing conditions, where

---

Abbreviations: DFT, density functional theory; CE, cluster expansion ; BEP, Brønsted–Evans–Polyani; GCMC, Grand Canonical Monte Carlo ; NN, nearest neighbor; OOBE, 1NN oxygen pair binding energy; TS, transition state; FCC, face-centered cubic; ML, monolayer; TOR, turn over rate.

* Corresponding author at: Department of Chemical and Biomolecular Engineering, University of Notre Dame, Notre Dame, IN 46556, USA.
E-mail address: wschneider@nd.edu (W.F. Schneider).

0021-9517/$ - see front matter © 2011 Elsevier Inc. All rights reserved.
doi:10.1016/j.jcat.2011.10.020

the metal surface has a high coverage of chemisorbed O. Over supported Pt particles, turnover rates (TORs) are observed to increase with particle size, and the greatest TORs are observed over the Pt (1 1 1) surface [34,35,37,38]. The hexagonal Pt (1 1 1) facet exposes threefold face-centered-cubic (FCC) sites that are the primary loci for atomic O adsorption. These adsorbed O_{fcc} interact repulsively, as manifested by both observed O surface orderings [39–42] and a decrease in average adsorption energy with increasing coverage [39,42–47]. In fact, this coverage-dependent O binding energy is integral to the efficacy of Pt as an NO oxidation catalyst: pristine Pt efficiently promotes NO_2 decomposition (the reverse of reaction (1)) rather than NO oxidation [39]. High pressure X-ray photoelectron spectroscopy experiments (XPS) and DFT-based transition state theory (TST) calculations [48,49] show that barriers to O_2 dissociative adsorption on Pt (1 1 1) are strongly sensitive to the presence of co-adsorbed O [48,50]:

$$O_2(g) + *(\theta) \overset{\text{rds}}{\rightarrow} 2O_{fcc} \tag{2}$$

where $*(\theta)$ represents some coverage-sensitive dissociation site. Based on kinetic observations, O_2 adsorption and accommodation have been proposed to be rate-limiting in NO oxidation over both single-crystal and supported catalysts [33–35,37,38]. In contrast, conversion of NO to NO_2

$$NO(g) + O_{fcc} \overset{K}{\rightleftharpoons} NO_2(g) \tag{3}$$

has a modest activation barrier that is largely insensitive to the presence of co-adsorbed O [48], consistent with the reaction being in quasi-equilibrium under catalytically interesting conditions [33–36]. Observed NO oxidation apparent activation energies and rate orders over Pt (1 1 1) are qualitatively similar to the supported Pt catalysts, but exhibit more subtle dependences on reaction conditions [37,38].

The essence of our CE-enabled "basis site" approach to developing a coverage-dependent kinetic model of reactions (2) and (3) is illustrated in Fig. 1. O_2 adsorption and dissociation events are taken to occur at reaction, or basis, sites i distinguished by the local arrangement of O adsorbates. The steady-state rate is written as a sum over rates at these basis sites ($\tilde{r}_i$) weighted by the number density per area of these sites ($\tilde{s}_i$) at a given reaction condition [51]:

$$r(T, \mu_O, P_{O_2}) = \sum_i \tilde{r}_i(T, P_{O_2})\tilde{s}_i(T, \mu_O) \tag{4}$$

where $\tilde{s}_i$ contains all the information about the distribution of O adsorbates at a surface and is a function of temperature T and the chemical potential of O, μ_O. We take reaction (3) to be in quasi-equilibrium, so that μ_O is related to the NO and NO_2 pressures by [42]

$$\begin{aligned}\mu_O(T, P_{NO_2}, P_{NO}) &= \mu_{NO_2}(T, P_{NO_2}) - \mu_{NO}(T, P_{NO}) \\ &= G^{\circ}_{NO_2}(T, 1\,\text{bar}) - G^{\circ}_{NO}(T, 1\,\text{bar}) + k_B T \ln\frac{P_{NO_2}}{P_{NO}}\end{aligned} \tag{5}$$

where G° are standard state Gibbs free energies, taken from the NIST Chemistry WebBook [52], and k_B is the Boltzmann constant.

The $\tilde{s}_i$ are evaluated by averaging over equilibrium configurations of adsorbed O at catalytically relevant ranges of μ_O and T. We use supercell DFT calculations to parameterize an accurate cluster expansion of surface energies as a function of O configuration, σ [16,18,19,21–24,53]. Grand Canonical Monte Carlo (GCMC) simulations on this CE Hamiltonian provide equilibrium configurations as a function of temperature and oxygen chemical potential from which $\tilde{s}_i$ can be extracted.

The $\tilde{r}_i$ contain the site-specific rate information and can in principle be parameterized in any appropriate way. Here, we use DFT simulations to determine O_2 reaction pathways over a set of representative sites. We show that these microscopic reactions approximately follow a Brønsted–Evans–Polyani (BEP) relationship [54–56] and that this relationship allows site-specific activation energies $E_i^{\ddagger}$ to be extracted from the same CE.

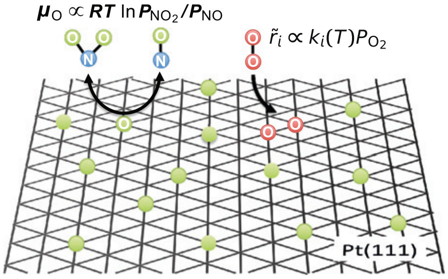

Fig. 1. NO oxidation model over Pt (1 1 1). NO_2 dissociation is equilibrated and sets the O chemical potential μ_O and O coverage; O_2 dissociation events occurs at rates $\tilde{r}_i(T, P_{O_2})$ whose rate constants $k_i(T)$ are determined by the local arrangement of O adsorbates.

This approach retains some of the simplicity of but goes beyond a mean-field model by taking advantage of the microscopic details accessible through DFT, CE, and GCMC simulations. As we show here, its efficiency allows steady-state rates to be evaluated over a large range of reaction conditions, allowing accurate evaluations of rate derivatives for comparison with experiment. We find that a model based on reactions (2) and (3) yields apparent activation energies and rate orders in good agreement with experiment for NO oxidation over Pt (1 1 1), supporting the validity of both the chemical model and computational approach. Further, the approach provides insights into the microscopic contributions to observed macroscopic kinetic properties.

2. Computational details

DFT calculations were performed within a plane wave, supercell approach using the Vienna ab initio Simulation Package (VASP) [57]. Interactions between frozen core and valence electrons were described with the projector augmented wave (PAW) method [58,59], and exchange and correlation were described using the Perdew–Wang-91 (PW91) implementation of the generalized gradient approximation (GGA) [60,61]. Plane waves were included to an energy cutoff of 400 eV. Gaussian electron smearing was used with a width of 0.1 eV. The Pt lattice constant was set to the computed bulk value of 3.986 Å [42]. The Pt (1 1 1) surface was modeled using four-layer slabs plus 12 Å of vacuum, with the bottom Pt layer fixed at the bulk positions. O_2 dissociation pathways were explored using a 4 × 4 4-layer supercell with a 3 × 3 × 1 Monkhorst–Pack **k**-point mesh [62]. Transition states (TSs) were located using a combination of climbing image nudged elastic band (CI-NEB) [63] and dimer [64] calculations and converged to 0.03 eV $Å^{-1}$. Subsequent vibrational frequency and CINEB calculations verified the identities of all TSs.

To parameterize the Pt (1 1 1)-O_{fcc} CE, the relaxed energies of fifty configurations spanning coverages from 0 to 1 monolayer (ML) O_{fcc} in supercells containing 1 to 8 FCC sites were evaluated. Configurational energies were evaluated with a Γ-centered **k**-point mesh [62] with at least 84.6 **k**-points/$Å^{-1}$ and expanded in one-, two- and many-body interaction terms using the Alloy Theoretic Automated Toolkit (ATAT) [22–24].

3. Results

As illustrated in Fig. 1, we seek to describe the steady-state kinetics of O_2 dissociation at a partially O-covered Pt (1 1 1) surface. The Pt (1 1 1) surface is susceptible to reconstructions at FCC O

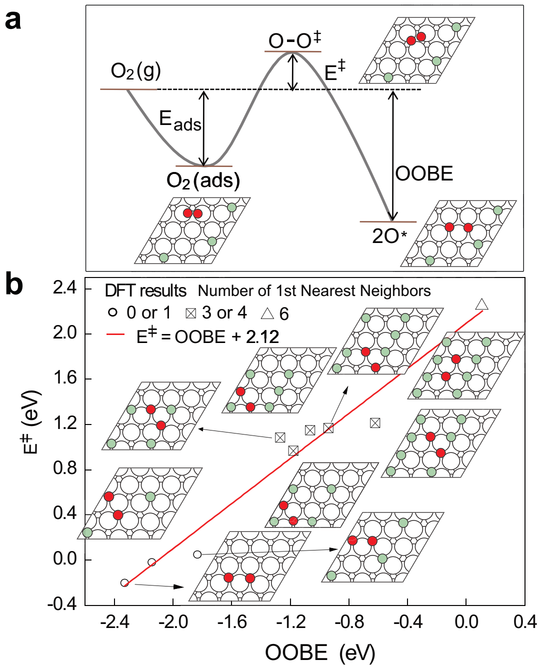

Fig. 2. (a) Schematic O_2 adsorption and dissociation potential energy surface. (b) DFT-calculated $E^{\ddagger}$ vs. final state (OOBE) binding energy for O_2 dissociation on O precovered Pt (111) slabs. Green and red dots indicate pre-adsorbed O and dissociated O_2, respectively.

coverage > 0.5 monolayer (ML) [65,66]; we restrict the analysis here to the non-reconstructed regime.

In a first set of calculations, we determined the dependence of the O_2 adsorption and dissociation pathway on the local dissociation environment. Fig. 2a shows a representative O_2 reaction energy profile on a surface containing several pre-adsorbed O indicated in green. O_2 (indicated in red) adsorbs molecularly in an atop-bridge-atop site and dissociates along a pathway in which two first-nearest-neighbor (1NN) vacant FCC O sites become occupied. O_2 is in an atop-hcp-bridge configuration at the TS, with an O–O bond distance of about 1.87 Å and an imaginary frequency of 311 cm^{-1}. Similar pathways are identified on a number of O-precovered Pt (111) 4 × 4 supercells with nominal coverages ranging from 0 to 1/2 ML FCC O. The actual dissociation pathways vary from case-to-case (as evidenced by O–O imaginary frequencies from 280 to 540 cm^{-1} and distances from 1.60 to 1.98 Å), as the dissociating O_2 seeks to minimize unfavorable adsorbate–adsorbate interactions at the TS. Fig. 2b plots the computed activation energy, ($E^{\ddagger}$, calculated relative to gas-phase O_2) against the net dissociated state binding energy (OOBE, also referenced to gas-phase O_2). The number of pre-adsorbed O 1NN to the dissociation site is found to have a strong influence on both energies. Dissociation is exothermic in all cases except those with the largest number of 1NNs; dissociation barriers range from negative in the presence of 0 or 1 1NNs to quite positive at higher neighbor numbers.

From Fig. 2b, the activation barriers and adsorption energies are approximately linearly correlated with slope near unity and intercept of 2.12 eV, consistent with a Brønsted–Evans–Polyani (BEP)-type relationship [49,54]. For the purposes of the model developed here, we identify a pair of vacant, neighboring FCC adsorption sites as a candidate dissociation site, i, and write

$$E_i^{\ddagger}(BEP) = \max[0, \mathrm{OOBE}_i + 2.12] \quad (6)$$

Negative activation energies are replaced by a zero energy barrier.

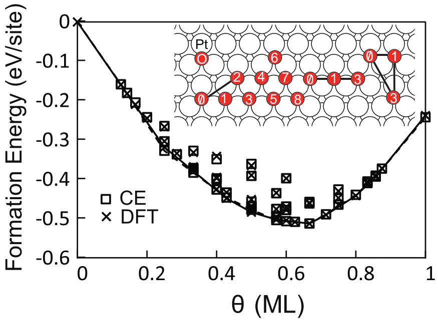

Fig. 3. CE-predicted vs. DFT-calculated formation energies $(E_f = (E(\sigma) - E(0) - \frac{n_O}{2}E_{O_2})/n_{FCC})$. The hull of ground states is connected with a line. Inset: eight two-body (between site 0 and sites i, e.g., 0–2 sites connected by line is the second nearest neighbor pair) and two three-body figures used in the CE.

These results illustrate the strong dependence of O_2 dissociation barriers and reaction energies on the local arrangement of co-adsorbates. To quantitatively model the configuration-dependent energetics, we turn to a cluster expansion of chemisorbed O on Pt (111). The CE expands the energy of a configuration of adsorbates σ in one-body, two-body, and higher order interactions [16–19,21–24,53]:

$$E(\sigma) = \sum_i c_0 + \sum_i c_i o_i + \sum_{i,j} c_{i,j} o_i o_j + \sum_{i,j,k} c_{i,j,k} o_i o_j o_k + \cdots \quad (7)$$

where the occupancy variables $o_i = -1$ or $+1$ if site i is empty or filled, respectively (i.e., following the Ising convention). The effective cluster interactions (ECIs, c) are selected to minimize a cross-validation (CV) score, or the ability of the expansion to predict the energies of configurations within the 50-configuration data set [21–24,53,67,68]. We found that a 12-term CE including the point, eight pair, and two three-body interactions produced a CV score of 5 meV/FCC site (Fig. 3). While the 1NN pair figure has the largest contribution to the overall CE, consistent with the strongly repulsive O–O interactions at this separation, the three-body interactions are essential to fit the adsorption energies and ground state configurations even qualitatively correctly; a two-body-only expansion has a CV score of 25 meV and cannot recover the prominent ground states at 1/4, 1/2, and 2/3 ML FCC O.

To determine the equilibrium distribution of O adsorbates at reaction conditions, we performed Grand Canonical Monte Carlo (GCMC) simulations using the CE Hamiltonian. Simulations were performed on a 42 × 42 periodic, hexagonal supercell, with temperatures ranging from 480 to 680 K and chemical potentials μ_O representative of those relevant to catalytic NO oxidation. Ten replicas were run at each condition. Random initial configurations were generated, and Monte Carlo moves performed until averaged coverages fluctuated less than 0.15%. The total MC attempts per FCC site ranged from 7000 to 30,000 depending on temperature. Statistics were then accumulated on the total O coverage $(\theta(\mu_O, T))$, on the distribution of vacant neighbor pair sites O_2 dissociation sites, which become the $\tilde{s}_i(\mu_O, T)$ of the kinetic model, and on the energy to occupy each candidate vacant neighbor pair dissociation site with two O atoms (OOBE_i). The last of these is determined by using the CE to evaluate the change in energy associated with a double occupancy variable flip at the reaction site:

$$\mathrm{OOBE}_i = E_{CE}(\sigma_i + \mathrm{OO}_{1NN}) - E_{CE}(\sigma_i) - E_{O_2} \quad (8)$$

Tests show that GCMC averaging was sufficient to converge the site-averaged activation energy (described below) to within 0.01 eV, less than the bin size of the OOBE distribution histogram.

Fig. 4 shows representative results at 600 K and chemical potentials corresponding to equilibrium coverages of 0.36 and

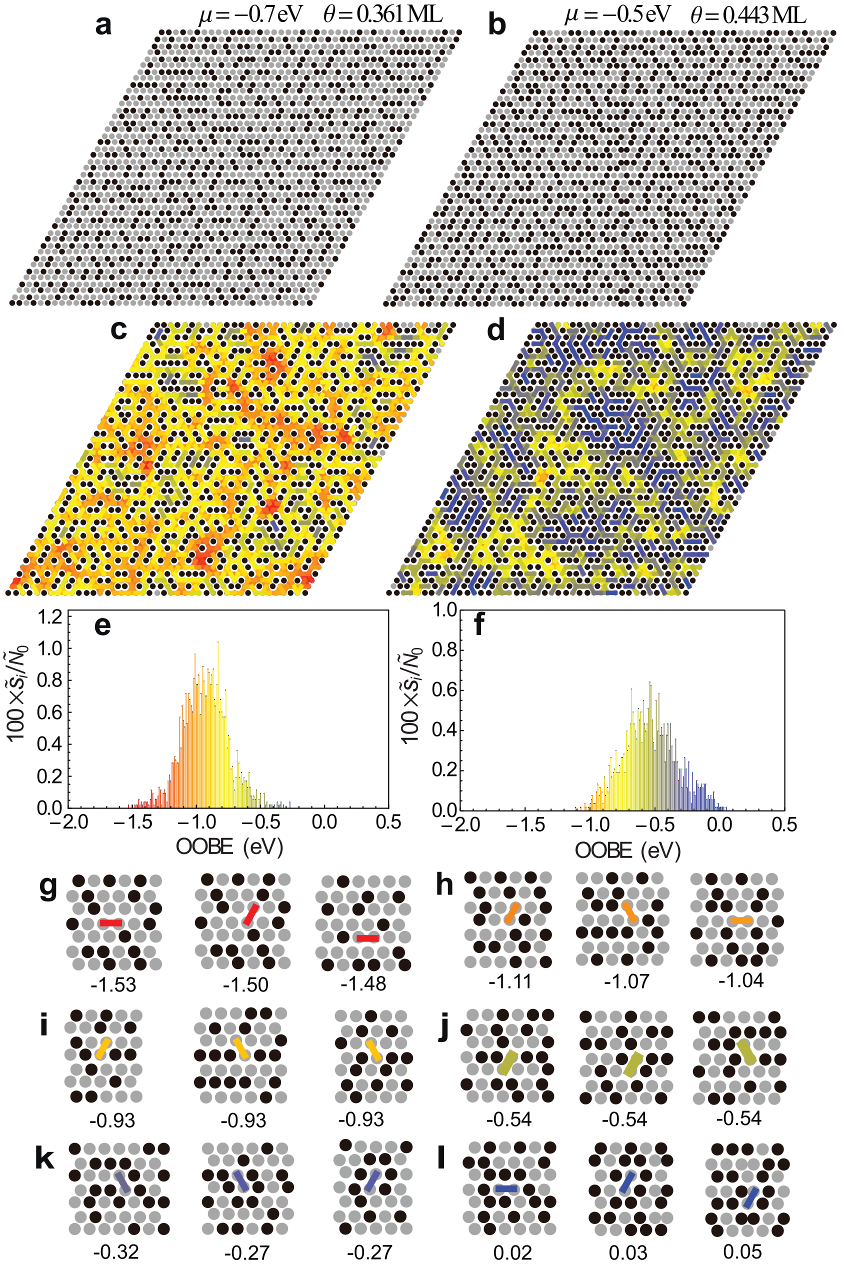

Fig. 4. (a and b) Representative snapshots of GCMC-generated O configurations at 600 K and two μ_O. (c and d) Same snapshots with vacant FCC site pairs color-coded by OOBE. Red to yellow colors indicate more exothermic and gray to blue less exothermic adsorption. (e) and (f) OOBE histograms from same snapshots, in 10 meV bins, normalized to the number of basis sites at zero coverage ($\tilde{N}_0$). Bins are color-coded to correspond with colors in (c) and (d). (g), (i), (k) Local configurations extracted from snapshot (a) of strong, intermediate, and weak binding divacancy sites. (h), (j), (l) Similar for snapshot (b). (For interpretation of the references to color in this figure legend, the reader is referred to the web version of this article.)

0.44 ML FCC O. Fig. 4a and b show typical snapshots from the GCMC simulations. The O adsorbates are seen to be essentially disordered at both conditions, although lines of filled and vacant sites are evident, which are precursors to the ground state ordered p (2×1) structure that is the ground state at 0.5 ML FCC O [16,42,44,53]. If the O were non-interacting, the distribution of adsorbates would be random, and the density of vacant 1NN pair reaction sites i would scale as $(1 - \theta_O)^2$, or 0.41 and 0.31 at $\theta_O = 0.36$ and 0.44 ML, respectively. Interactions cause the total density to decrease more rapidly, to 0.35 and 0.25 of the clean surface, respectively, at the conditions shown in the figure. These observations are a direct consequence of the short-range order (SRO) captured in the CE and Monte Carlo models. Because 1NN O pairs interact repulsively, an O is more likely than random statistics would say to be surrounded by vacancies and vice versa. Thus, the number of O-vac pairs is larger than the random (non-interacting) value, and the numbers of O–O and vacancy-vacancy pairs are smaller than the random values.

Not all of these 1NN vacant pairs are equivalent, as portrayed more clearly in the colored OOBE maps in Fig. 4c and d. Here, each neighbor vacancy pair is shaded according to the computed energy to occupy the site. Red to yellow colors indicate more exothermic and gray to blue less exothermic adsorption. Evident from these pictures is the shift from lower to higher energy reaction sites when going from the lower to the higher coverage conditions.

Fig. 4e and f show computed 1NN OOBE histograms, collected in 10 meV bins, averaged over the GCMC simulations, and color-coded to match Fig. 4c and d. The histograms are normalized to the total number of vacant pairs on the same-sized adsorbate-free surface. These normalized $\tilde{s}_i$ distributions are essentially unimodal with means of -0.93 and -0.54 eV, respectively, and standard deviations of 0.34 and 0.32 eV, respectively. Fig. 4i and j shows close-ups of representative local configurations with OOBEs near the mean values. The number of O 1NN to these typical sites is about $3 \sim 4$ and 5, respectively.

Based on the computed dissociation pathways and BEP relationship, the sites expected to contribute most significantly to O_2 dissociation are those that bind the final products most strongly. The strongest binding sites that appear in Fig. 4a and b are expanded in Fig. 4g and h. Because repulsive 1NN interactions have the largest influence on adsorption energies, the candidate reaction sites have locally low coverage. Site (g) and others extracted near 0.36 ML O have approximately two first-nearest-neighbors; in site (h) and similar near 0.44 ML O, the number increases to three or four. Essentially, no vacant FCC pair binding sites with zero neighbors are present at these conditions. Finally, the high-energy tails of the OOBE distribution are illustrated in Fig. 4k and l. These sites contain about $6 \sim 7$ and 7 1NN Os, respectively. The OOBE difference now mainly comes from the second NN or further interactions. At both conditions, there are thus a large variety of candidate reaction sites, and the most and least reactive sites are seen to be distinct minorities of the total.

The OOBE histograms provide all the information necessary to calculate steady-state O_2 dissociation rates. Site-specific rates are written in an Arrhenius form:

$$\tilde{r}_i(T, P_{O_2}) = A(T, P_{O_2}) \exp\left(-\frac{E_i^{\ddagger}(BEP)}{k_B T}\right) \tag{9}$$

The pre-exponential factor A for all sites in the indirect adsorption approximation is

$$A(T, P_{O_2}) = F_{O_2}(T, P_{O_2})\kappa \tag{10}$$

where $F_{O_2}(T, P_{O_2})$ is the flux per area of O_2 to the surface and κ is an orientational sticking factor that we arbitrarily set to 1/6 [3,69]. Eqs. (4), (8) and (9) provide total rates for any value of T and μ_O. Results are shown for six temperatures from 480 to 680 K and 12 different chemical potentials incremented by 0.05 eV, all at P_{O_2} of 0.1 bar, in Fig. 5a. For making connection to NO oxidation kinetics, it is useful to relate μ_O to the NO_2 to NO pressure ratio through Eq. (5). NO oxidation rates are plotted as the natural log turnover rate (rate normalized by the exposed platinum, TOR = $2r/L$, where L = 1.45 Pt Å^{-2}) vs. the natural log of this pressure ratio. The computed values encompass ranges reported in experimental measurements of NO oxidation TORs over Pt (111) [38]. Absolute TORs vary over approximately eight orders of magnitude, increasing with increasing temperature and decreasing with increasing pressure ratio and coverage.

While absolute rates are sensitive to the absolute DFT-computed reaction barriers and prefactor details and should be compared only with caution to experiment, derivatives of the rates provide more insight into the effects that control reactivity. We first consider the apparent activation energy at constant reactant pressures, given by

$$E_{app}^{\ddagger} = -k_B \left(\frac{\partial \ln r}{\partial (1/T)}\right)_{\frac{P_{NO_2}}{P_{NO}}, P_{O_2}} \tag{11}$$

It is convenient to take the temperature derivative at $\mu_O = -0.7$ eV, where $\ln(P_{NO_2}/P_{NO}) = 1.16$ over all temperatures simulated (Fig. 5). The fraction of occupied FCC O sites (θ_O) is about 0.36 ML at this chemical potential and range of temperatures, and from a linear fit in $1/T$, we obtain $E_{app}^{\ddagger} = 77 \pm 3$kJ mol^{-1}. The computed rates vs. $\ln(P_{NO_2}/P_{NO})$ form nearly parallel lines, and thus, the computed apparent activation energy is roughly insensitive to this pressure ratio. Numerical fits of the rate data allow us to estimate the temperature derivative at other conditions. At a more modest $\ln(P_{NO_2}/P_{NO}) = -2.41$, or $P_{NO_2}/P_{NO} = 0.09$, the steady-state coverage $\theta_O \approx 0.28$ and $E_{app}^{\ddagger} \approx 69$kJ mol^{-1}; at a relatively large $\ln(P_{NO_2}/P_{NO}) = 6.31$, or $P_{NO_2}/P_{NO} = 550$, the steady-state coverage is $\theta_O \approx 0.47$ and $E_{app}^{\ddagger} \approx 87$kJ mol^{-1}. It is interesting to note that the oxygen coverage varies less than 0.2ML over this very large range of pressure ratios, and that the coverages are only weakly T-dependent [42]. These absolute apparent activation energies are slightly less than the 82 kJ mol^{-1} reported at $P_{NO_2}/P_{NO} = 0.57$ for Pt dispersed on high surface area supports [33] and slightly greater than the 65 ± 10 kJ mol^{-1} reported over Pt (111) at $P_{NO_2}/P_{NO} = 1.1$ [38]. The increase in $E_{app}^{\ddagger}$ with P_{NO_2}/P_{NO} is in qualitative agreement with the trend observed over Pt (111) [38].

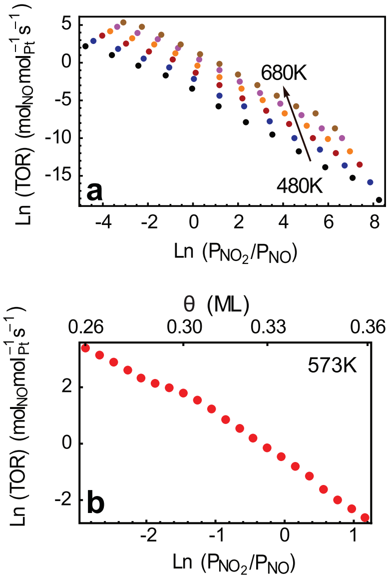

Fig. 5. (a) Model NO oxidation TOR vs. $\ln(P_{NO_2}/P_{NO})$. Temperatures range from 480 to 680 K in 40 K increments, as indicated by colored points. $P_{O_2} = 0.1$ bar. (b) Model TOR over narrower range of pressures, at 573 K.

To understand the physical origins of the modeled apparent activation energy, it is helpful to decompose the contributions of various sites to the overall computed rate. Fig. 6 compares computed site-densities $\tilde{s}_i$ and relative rate contributions from basis sites ($\tilde{r}_i$ weighted by site density $\tilde{s}_i$) as a function of $E^{\ddagger}$, mapped from the OOBE using Eq. (8). The histograms are collected at various T and μ_O corresponding to a range of coverages from $\theta_O = 0.31$ to 0.48 ML. It is evident from the plots that the statistically most common sites, where the sites densities $\tilde{s}_i$ are maximized, contribute negligibly to the overall rate; rather, the kinetically-relevant sites are the relatively uncommon and locally low-coverage ones, like those shown in Fig. 4g and h, on the low energy side of the OOBE distribution. Further, these kinetically-relevant sites change with reaction conditions, moving up or down in energy with the overall site distribution. Moving across the figure at any fixed O chemical potential and increasing temperatures, the total O coverages are seen to increase slowly, the height of the site-density and weighted site-density histograms $\tilde{s}_i$ and $\tilde{r}_i\tilde{s}_i$ to decrease slowly, but the activation energy range spanned by the sites to be roughly invariant. Varying temperature has a modest effect on the types of reaction sites contributing to the overall rate. At constant temperature and increasing O coverage, going down any column, the picture is

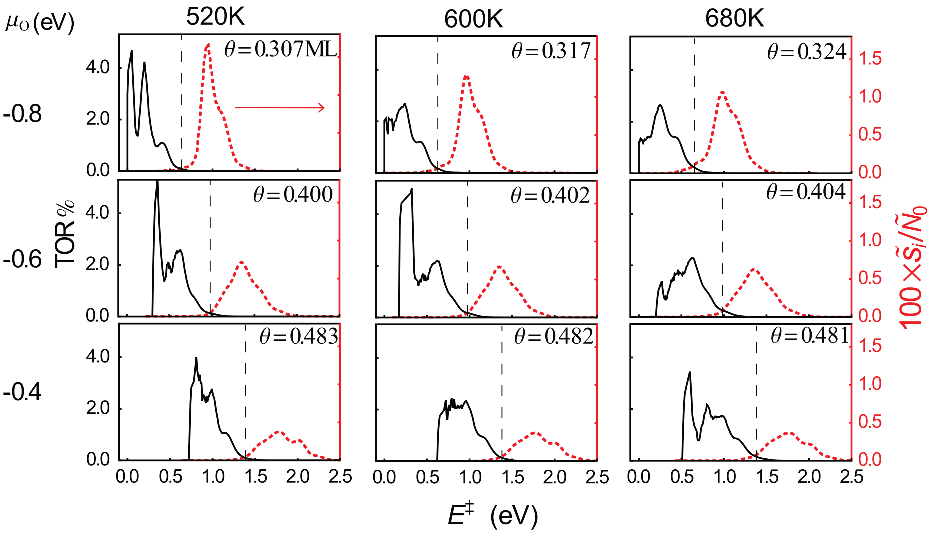

Fig. 6. O_2 dissociation site densities $\tilde{s}_i$ normalized to zero coverage (thick dashed lines and right axes) and percent rate contributions $\tilde{r}_i\tilde{s}_i$/TOR (solid lines and left axes) vs. $E^\ddagger$ over a matrix of T and μ_O values. Vertical dashed lines indicate site-average activation energies, $\bar{E}^\ddagger$.

different: O coverages increase substantially with increasing μ_O, and the histograms diminish in size and shift to higher activation energy. The types of sites available for O_2 dissociation are a strong function of coverage over this range of conditions.

To quantify these ideas, we define the site-averaged rate $\bar{r}$ and activation energy $\bar{E}^\ddagger$ according to

$$r(T,\mu_O,P_{O_2}) = \sum_i \tilde{r}_i\tilde{s}_i = \bar{r}\sum_i \tilde{s}_i \tag{12}$$

$$\bar{r} = A(T,P_{O_2})e^{-\bar{E}^\ddagger(T,\mu_O)/k_BT} \tag{13}$$

Prefactors are taken to be site-independent, then by rearrangement

$$\begin{aligned}\bar{E}^\ddagger(T,\mu_O) &= -k_BT\ln\frac{r(T,\mu_O,P_{O_2})}{A(T,P_{O_2})\sum_i \tilde{s}_i(T,\mu_O)} \\ &= -k_BT\ln\frac{\sum_i \tilde{s}_i(T,\mu_O)e^{-E_i^\ddagger/k_BT}}{\sum_i \tilde{s}_i(T,\mu_O)}\end{aligned} \tag{14}$$

By temperature differentiation of Eq. (12) at constant μ_O, the apparent activation energy can be related to the site-averaged activation energy and its temperature derivative:

$$\begin{aligned}E^\ddagger_{\mathrm{app}}(T,\mu_O) = \bar{E}^\ddagger(T,\mu_O) + \frac{1}{T}\left(\frac{\partial\bar{E}^\ddagger}{\partial 1/T}\right)_{\mu_O} - k_B\left(\frac{\partial\ln\sum_i\tilde{s}_i}{\partial 1/T}\right)_{\mu_O} \\ - k_B\left(\frac{\partial\ln A(T)}{\partial 1/T}\right)_{P_{O_2}}\end{aligned} \tag{15}$$

Site-averaged activation energies calculated using Eq. (14) are indicated by the vertical dashed lines in each panel of Fig. 6; in general, they are in the strong binding tails of the site-density histograms. The dominant contribution to $E^\ddagger_{\mathrm{app}}$ is this site-averaged activation energy. The contribution from the temperature derivative of $\bar{E}^\ddagger$ is smaller (the second term in Eq. (15), ~0.1 eV) as can be seen from the modest change in $\bar{E}^\ddagger$ across temperatures from 520 to 680 K at a given μ_O. The last two terms (change in total coverage and in prefactor) contribute less than 0.1 eV [49]. Because μ_O has a temperature dependence itself through Eq. (5), the two leading terms in Eq. (15) vary more when calculated at constant pressure ratio rather than μ_O, but the general conclusion that the behavior of $\bar{E}^\ddagger$ dominates the apparent activation energy remains unchanged.

We next consider the apparent rate dependence on the P_{NO_2}/P_{NO} ratio, which via reaction (3) controls the O coverage. One can define an apparent rate order with respect to the pressure ratio:

$$n_O = \left(\frac{\partial\ln r}{\partial\ln(\frac{P_{NO_2}}{P_{NO}})}\right)_{T,P_{O_2}} = k_BT\left(\frac{\partial\ln r}{\partial\mu_O}\right)_{T,P_{O_2}} \tag{16}$$

From Fig. 5a, the log rate varies nearly linearly with log pressure ratio, with a slope between −1 and −2. The parallel TOR feature shown in Fig. 5a implies similar reaction orders at other temperatures. The full range of pressure ratios is quite large here; to refine the analysis, we calculated rates at 573 K over a finer grid of O chemical potentials corresponding to P_{NO_2}/P_{NO} pressure ratios between 0.05 and 3.22, shown in Fig. 5b. A slope change is evident between 0.27 and 0.31 ML, as the surface transitions from one dominated by an ordered $p(2\times2)$-O structure at $\frac{1}{4}$ ML to a disordered one above ~0.3 ML. The reaction order obtained by numerical differentiation is around $-1.2\sim-0.9$ at lower pressure ratios (NO_2:NO < 0.3), increasing to −1.6 at NO_2:NO ≈ 0.6 and stabilizing around that number for higher ratios. Observed rate orders over a Pt (1 1 1) single crystal similarly vary as a function of the pressure ratio, starting from −0.9 to −1.1 at NO_2:NO < 0.3 and then monotonically decreasing to −2 at NO_2:NO ≈ 1.1 [38].

The rate order can be decomposed using a procedure similar to that described for the apparent activation energy:

$$n_O = k_BT\left(\frac{\partial\ln\sum_i\tilde{s}_i}{\partial\mu_O}\right)_T - \left(\frac{\partial\bar{E}^\ddagger}{\partial\mu_O}\right)_T \tag{17}$$

The first term corresponds to the change in total available reaction sites with μ_O. Over the range of reaction conditions considered in Fig. 4, for instance, its contribution is only on the order of −0.1. As shown in Fig. 6, however, $\bar{E}^\ddagger(\mu_O,T)$ is a strong function of μ_O, i.e., the *types* of sites that contribute to reactivity change with O coverage, and this dependence dominates the rate orders on Pt (1 1 1) over the range of conditions considered here.

The NO oxidation rate order n_O is reported to be near unity when measured over supported Pt catalysts over a range of P_{NO_2}/P_{NO} similar to the narrower region modeled here [33–36]. This behavior has been interpreted by these authors in terms of a Langmuir–Hinshelwood model in which reaction occurs at a single kinetically-relevant site, $*$, independent of coverage, O_2 adsorption at this site is rate-limiting, and subsequent O_2^* dissociation is rapid:

$$O_2 + 2* \xrightarrow{\text{rds}} O_2^* + * \xrightarrow{\text{fast}} 2O^* \qquad (18)$$

The DFT and basis site model results here present a different picture over Pt (111), in which the kinetically-relevant sites change in concert with coverage. This coverage- and site-sensitive dissociative O_2 adsorption mechanism yields apparent activation energies and orders similar to those observed over supported catalysts. Further work is necessary to understand how the model results here translate to the structurally more complicated supported catalyst motif.

4. Conclusions

We have taken advantage of a first-principles-based cluster expansion (CE) to incorporate accurate adsorbate–adsorbate interactions into a lattice-based "basis site" model of rate-limiting O_2 dissociation at a Pt (111) surface, a model for catalytic NO oxidation at this surface. The CE provides access both to predictions of available reaction sites under realistic conditions and, through a BEP, to reaction rates at those sites. The model predicts experimentally observed O coverages and recovers NO oxidation rates and rate derivatives in good agreement with experiment. The results indicate that reaction rates are dominated by a minority of locally low-coverage sites, and the precise identity of these kinetically-relevant sites changes over the range of interesting reaction conditions on this surface.

The approach described here bridges empirical mean-field and more computationally demanding kinetic Monte Carlo approaches to reaction rate modeling. The specific model described here is simplified in a number of respects: the coverage of any species other than O is neglected, the O_2 dissociation BEP may over-simplify the actual O_2 dissociation dynamics, surface reconstructions that appear at higher coverages are not described, and the ordered (111) model is not well representative of the high surface area catalysts of greatest practical interest. The modeling approach is flexible enough to incorporate many of these phenomenon, however, and further generalizations are the topic of on-going work.

Acknowledgments

We thank Dr. Rachel Getman, Dr. Andrew Smeltz, Prof. Fabio Ribeiro, Prof. Nick Delgass, Dr. Jean-Sabin McEwen, Dr. Zhengzheng Chen, and Mr. Jason Bray for helpful discussions. We also acknowledge computational resources provided by the Center for Research Computing at the University of Notre Dame and the Center for Nanoscale Materials at Argonne National Laboratory. Financial support for this work was provided the US Department of Energy under Grant DE-FG02–06ER15839 and by the National Science Foundation under Contract Nos. CBET-0731020 and CBET-0730841.

References

[1] M. Neurock, J. Catal. 216 (2003) 73–88.
[2] J.K. Nørskov, T. Bligaard, J. Rossmeisl, C.H. Christensen, Nat. Chem. 1 (2009) 37–46.
[3] I. Chorkendorff, J.W. Niemantsverdriet, Concepts of Modern Catalysis and Kinetics, second ed., Wiley-VCH, 2007.
[4] V.P. Zhdanov, Surf. Sci. Rep. 12 (5) (1991) 185–242.
[5] D.Y. Murzin, Ind. Eng. Chem. Res. 44 (2005) 1688–1697.
[6] J.J. Lukkien, J.P.L. Segers, P.A.J. Hilbers, R.J. Gelten, A.P.J. Jansen, Phys. Rev. E 58 (1998) 2598–2610.
[7] E.W. Hansen, M. Neurock, Surf. Sci. 441 (1999) 410–424.
[8] E.W. Hansen, M. Neurock, Chem. Eng. Sci. 54 (1999) 3411–3421.
[9] D. Mei, Q. Ge, M. Neurock, L.D. Kieken, J. Lerou, Mol. Phys. 102 (2004) 361–369.
[10] S. Ovesson, B.I. Lundqvist, W.F. Schneider, A. Bogicevic, Phys. Rev. B 71 (11) (2005) 115406.
[11] M. Stamatakis, D.G. Vlachos, J. Chem. Phys. 134 (2011) 214115.
[12] D.-J. Liu, J.W. Evans, ChemPhysChem 11 (10) (2010) 2174–2181.
[13] D.-J. Liu, J.W. Evans, J. Chem. Phys. 124 (15) (2006) 154705.
[14] S. Payne, J.-S. McEwen, H. Kreuzer, D. Menzel, Surf. Sci. 594 (1–3) (2005) 240–262.
[15] C. Stampfl, H.J. Kreuzer, S.H. Payne, H. Pfnür, M. Scheffler, Phys. Rev. Lett. 83 (1999) 2993–2996.
[16] H. Tang, A. Van der Ven, B.L. Trout, Phys. Rev. B 70 (4) (2004) 045420.
[17] H. Tang, A. Van Der Ven, B.L. Trout, Mol. Phys. 102 (2004) 273–279.
[18] B.C. Han, A. Van der Ven, G. Ceder, B.-J. Hwang, Phys. Rev. B 72 (20) (2005) 205409.
[19] S.D. Miller, J.R. Kitchin, Mol. Simul. 35 (2009) 920–927.
[20] D. Lerch, O. Wieckhorst, L. Hammer, K. Heinz, S. Müller, Phys. Rev. B 78 (12) (2008) 121405.
[21] D. Lerch, O. Wieckhorst, G. Hart, R. Forcade, S. Müller, Modell. Simul. Mater. Sci. Eng. 17 (2009) 055003.
[22] A. Van de Walle, G. Ceder, J. Phase Equilibr. 23 (4) (2002) 348–359.
[23] A. Van de Walle, M. Asta, G. Ceder, Calphad 26 (4) (2002) 539–553.
[24] J. Sanchez, F. Ducastelle, D. Gratias, Physica A 128 (1–2) (1984) 334–350.
[25] Y. Zhang, K. Reuter, Chem. Phys. Lett. 465 (4–6) (2008) 303–306.
[26] K. Reuter, C. Stampfl, M. Scheffler, Handbook of Materials Modeling, vol. 1, Springer, 2004, p. 24.
[27] S. Piccinin, C. Stampfl, Phys. Rev. B 81 (15) (2010) 155427.
[28] C. Stampfl, Phase Transit. 80 (4/5) (2007) 311–332.
[29] C. Stampfl, Catal. Today 105 (1) (2005) 17–35.
[30] J.-S. McEwen, A. Eichler, J. Chem. Phys. 126 (9) (2007) 094701.
[31] T. Franz, F. Mittendorfer, J. Chem. Phys. 132 (19) (2010) 194701.
[32] L. Olsson, H. Persson, E. Fridell, M. Skoglundh, B. Andersson, J. Phys. Chem. B 105 (2001) 6895–6906.
[33] S. Mulla, N. Chen, W. Delgass, W. Epling, F. Ribeiro, Catal. Lett. 100 (2005) 267–270.
[34] S. Mulla, N. Chen, L. Cumaranatunge, G. Blau, D. Zemlyanov, W. Delgass, W. Epling, F. Ribeiro, J. Catal. 241 (2) (2006) 389–399.
[35] B.M. Weiss, E. Iglesia, J. Phys. Chem. C 113 (30) (2009) 13331–13340.
[36] D. Bhatia, R.W. McCabe, M.P. Harold, V. Balakotaiah, J. Catal. 266 (1) (2009) 106–119.
[37] A. Smeltz, R. Getman, W. Schneider, F. Ribeiro, Catal. Today 136 (1–2) (2008) 84–92.
[38] A.D. Smeltz, W.N. Delgass, F.H. Ribeiro, Langmuir 26 (21) (2010) 16578–16588.
[39] D.H. Parker, M.E. Bartram, B.E. Koel, Surf. Sci. 217 (3) (1989) 489–510.
[40] J.L. Gland, B.A. Sexton, G.B. Fisher, Surf. Sci. 95 (2–3) (1980) 587–602.
[41] G. Ertl, Angew. Chem. Int. Ed. 47 (2008) 3524–3535.
[42] R.B. Getman, Y. Xu, W.F. Schneider, J. Phys. Chem. C 112 (26) (2008) 9559–9572.
[43] N. Saliba, Y.-L. Tsai, C. Panja, B. Koel, Surf. Sci. 419 (2–3) (1999) 79–88.
[44] J.F. Weaver, J.-J. Chen, A.L. Gerrard, Surf. Sci. 592 (1–3) (2005) 83–103.
[45] C. Campbell, G. Ertl, H. Kuipers, J. Segner, Surf. Sci. 107 (1) (1981) 220–236.
[46] A. Eichler, F. Mittendorfer, J. Hafner, Phys. Rev. B 62 (7) (2000) 4744–4755.
[47] P. Légaré, Surf. Sci. 580 (1–3) (2005) 137–144.
[48] R.B. Getman, W.F. Schneider, A.D. Smeltz, W.N. Delgass, F.H. Ribeiro, Phys. Rev. Lett. 102 (2009) 076101.
[49] R.B. Getman, W.F. Schneider, ChemCatChem 2 (11) (2010) 1450–1460.
[50] D.J. Miller, H. Öberg, L.-Å. Näslund, T. Anniyev, H. Ogasawara, L.G.M. Pettersson, A. Nilsson, J. Chem. Phys. 133 (22) (2010) 224701.
[51] K. Honkala, A. Hellman, I.N. Remediakis, A. Logadottir, A. Carlsson, S. Dahl, C.H. Christensen, J.K. Nørskov, Science 307 (5709) (2005) 555–558.
[52] D. Burgess, Thermochemical Data, in: NIST Chemistry WebBook, NIST Standard Reference Database Number 69, National Institute of Standards and Technology, Gaithersburg MD, 20899, 2011, <http://webbook.nist.gov> (retrieved 06.07.11).
[53] D.J. Schmidt, W.F. Schneider, W. Chen, C. Wolverton, J. Chem. Theory Comp., submitted fot publication.
[54] J.K. Nørskov, T. Bligaard, A. Logadottir, S. Bahn, L.B. Hansen, M. Bollinger, H. Bengaard, B. Hammer, Z. Sljivancanin, M. Mavrikakis, Y. Xu, S. Dahl, C.J.H. Jacobsen, J. Catal. 209 (2) (2002) 275–278.
[55] R.A.v. Santen, M. Neurock, S.G. Shetty, Chem. Rev. 110 (4) (2010) 2005–2048.
[56] S. Wang, B. Temel, J. Shen, G. Jones, L. Grabow, F. Studt, T. Bligaard, F. Abild-Pedersen, C. Christensen, J. Nørskov, Catal. Lett. 141 (2011) 370–373.
[57] G. Kresse, J. Furthmüller, Comput. Mater. Sci. 6 (1) (1996) 15–50.
[58] P.E. Blöchl, Phys. Rev. B 50 (24) (1994) 17953–17979.
[59] G. Kresse, D. Joubert, Phys. Rev. B 59 (3) (1999) 1758–1775.
[60] J.P. Perdew, J.A. Chevary, S.H. Vosko, K.A. Jackson, M.R. Pederson, D.J. Singh, C. Fiolhais, Phys. Rev. B 46 (11) (1992) 6671–6687.
[61] J.P. Perdew, Y. Wang, Phys. Rev. B 45 (23) (1992) 13244–13249.
[62] H.J. Monkhorst, J.D. Pack, Phys. Rev. B 13 (12) (1976) 5188–5192.
[63] G. Henkelman, H. Jonsson, J. Chem. Phys. 111 (15) (1999) 7010–7022.
[64] G. Henkelman, B.P. Uberuaga, H. Jonsson, J. Chem. Phys. 113 (22) (2000) 9901–9904.
[65] S.P. Devarajan, J.A. Hinojosa Jr., J.F. Weaver, Surf. Sci. 602(19) (2008) 3116 – 3124.
[66] J.M. Hawkins, J.F. Weaver, A. Asthagiri, Phys. Rev. B 79 (12) (2009) 125434.
[67] V. Blum, G.L.W. Hart, M.J. Walorski, A. Zunger, Phys. Rev. B 72 (16) (2005) 165113.
[68] J. Shao, J. Am. Stat. Assoc. 88 (422) (1993) 486–494.
[69] A.A. Gokhale, S. Kandoi, J.P. Greeley, M. Mavrikakis, J.A. Dumesic, Chem. Eng. Sci. 59 (22–23) (2004) 4679.